Priyanshu Agarwal
Mechanical Engineering Department,
The University of Texas at Austin,
Austin, TX 78712
e-mail: mail2priyanshu@utexas.edu

Richard R. Neptune
John T. MacGuire Professor
Mem. ASME
Mechanical Engineering Department,
The University of Texas at Austin,
Austin, TX 78712
e-mail: rneptune@mail.utexas.edu

Ashish D. Deshpande[1]
Assistant Professor
Mem. ASME
Mechanical Engineering Department,
The University of Texas at Austin,
Austin, TX 78712
e-mail: ashish@austin.utexas.edu

A Simulation Framework for Virtual Prototyping of Robotic Exoskeletons

A number of robotic exoskeletons are being developed to provide rehabilitation interventions for those with movement disabilities. We present a systematic framework that allows for virtual prototyping (i.e., design, control, and experimentation (i.e. design, control, and experimentation) of robotic exoskeletons. The framework merges computational musculoskeletal analyses with simulation-based design techniques which allows for exoskeleton design and control algorithm optimization. We introduce biomechanical, morphological, and controller measures to optimize the exoskeleton performance. A major advantage of the framework is that it provides a platform for carrying out hypothesis-driven virtual experiments to quantify device performance and rehabilitation progress. To illustrate the efficacy of the framework, we present a case study wherein the design and analysis of an index finger exoskeleton is carried out using the proposed framework.
[DOI: 10.1115/1.4033177]

1 Introduction

Clinical studies have shown that physical therapy with robotic exoskeletons has the potential to increase sensorimotor cortex activity after chronic stroke, which results in improved limb motor function [1–4]. However, designing effective exoskeletons is challenging and requires overcoming several technical challenges in a number of areas including actuators, sensors, physical human–robot interaction, and control based on the user intent [5–8]. In addition, accounting for the complex movement biomechanics and specific goals of the physical therapy (e.g., improve impaired limb range of motion, strength, and function) are also essential. Specific design requirements range from the physical hardware design (e.g., selection of the architecture and method to attach to the subject) to software-based control (e.g., impedance-based [9] and electromyography (EMG)-based or adaptive assist-as-needed control [10,11]).

A major limitation of the current practices for the design of robotic exoskeletons is that the dynamics, biomechanics, and neuromuscular controls of the human body are either ignored [12] or greatly simplified [13–16]. Simplifications can make it difficult to understand the influence of the exoskeleton on the musculoskeletal system and lead to suboptimal designs. Since exoskeletons are in close physical contact with the subjects, a synergistic approach that accounts for the coupled dynamic human–exoskeleton system is needed to ensure optimal performance.

In engineering design, computer-based functional physical simulations are commonly used for iterative refinement of products early in the design stage in order to reduce cost and improve performance [17]. A number of tools have been developed for musculoskeletal analyses over the past two decades including software for interactive musculoskeletal modeling [18], OpenSim [19], AnyBody modeling system [20], LifeModeler [21], and virtual interactive musculoskeletal system [22]. These tools have been used to analyze the coupled human–exoskeleton systems using musculoskeletal analyses [23–26]. However, these studies have been problem specific and analyzed or optimized with ad hoc objective functions without developing a comprehensive understanding of how the various performance measures affect the exoskeleton design and control performance. Without this understanding, it is difficult to predict what needs to be modified in order to improve the coupled system performance. Thus, a simulation framework that includes the musculoskeletal system coupled with the exoskeleton is needed to design and analyze the combined human–exoskeleton system, evaluate its performance, and perform virtual experiments to improve the design performance.

In this work, we develop a generalizable framework that allows for the simultaneous modeling of the exoskeleton hardware and the musculoskeletal system in order to optimize exoskeleton designs to improve rehabilitation outcomes. Specifically, we integrate computational musculoskeletal analyses with simulation-based design techniques to iteratively optimize the performance of a robotic exoskeleton using biomechanical, design, and controller performance measures. To illustrate the effectiveness of the proposed framework, we present a case study on virtual prototyping of an index finger exoskeleton and virtual experiments where different pathologies are simulated to illustrate how the degree of disability and rehabilitation recovery can be quantified. We have presented portions of this work in Refs. [27–29].

2 Overview of Virtual Prototyping Framework

Below, we present the framework to develop and refine hardware design and control algorithms for robotic exoskeletons that are in close contact with the human user. We introduce three types of measures to assess performance of the coupled human–exoskeleton model: (I) *Biomechanical measures* that include musculoskeletal quantities (e.g., joint reaction forces, muscle forces, and metabolic power consumption, etc.), (II) *Morphological measures* that are derived from the physical design (e.g., structural configuration, link lengths, stiffness, etc.) of the exoskeleton (e.g., coupled system range of motion, stability, controllability, etc.), and (III) *Controller measures* that describe the performance of the exoskeleton controller (e.g., steady-state tracking error, response time, maximum overshoot, etc.).

The following steps summarize the proposed framework (Fig. 1):

Step 1 (*Initial modeling*)*:* Develop an initial coupled exoskeleton–limb musculoskeletal model that captures the kinematics and dynamics of the coupled system along with the dynamics of the musculotendon actuators. In addition, develop a controller for the exoskeleton and identify appropriate models for the sensors and actuators in the exoskeleton.

Step 2 (*Performance measure identification*)*:* Identify the critical questions related to the coupled system performance. This will

[1]Corresponding author.

Manuscript received June 29, 2015; final manuscript received March 21, 2016; published online April 27, 2016. Assoc. Editor: Paul Rullkoetter.

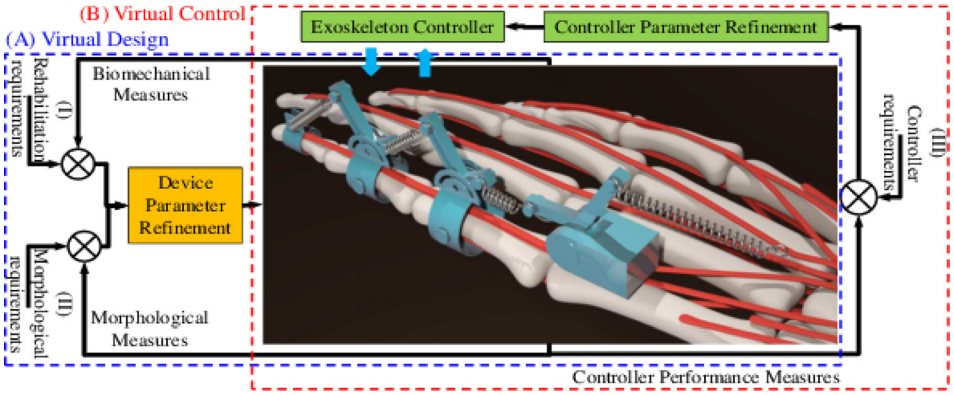

Fig. 1 Virtual prototyping framework illustrating the virtual design and control of an index finger exoskeleton using biomechanical, morphological, and controller performance measures

include identification of the key biomechanical, morphological, and controller measures that affect the coupled system performance. In addition, identify a nominal motion trajectory for the coupled exoskeleton–limb model based on the desired rehabilitation movement for which the exoskeleton design and control is optimized.

Step 3 (*Model fidelity*)*:* Improve the coupled exoskeleton–limb model fidelity by optimizing kinematic and dynamic parameters of the human limb and the exoskeleton using the experimental measurements. For example, the muscle moment arm data collected from cadaver studies can be used to obtain better estimates of the muscle routing in the musculoskeletal model. Also, initial estimates of the inertial parameters of the model can be obtained using a computer-aided design (CAD) model of the device. This step can also account for subject-specific customization of the coupled model.

Step 4 (*Virtual design*)*:* Carry out a virtual design by iteratively optimizing biomechanical and/or morphological performance measures while reproducing the nominal motion trajectory. This includes studying the effects of variability, determining the best geometries for performance (e.g., lower torques with improved controllability), and examining relationships between form and function (e.g., improved biomechanical compatibility). We set up the design optimization problem by coupling parametric models with functional simulation tools.

Step 5 (*Virtual control*)*:* Carry out virtual control by iteratively developing and refining control algorithms for the coupled system. The exoskeleton controller parameters can be tuned to optimize the performance for the desired motion trajectory. Once the initial design of the exoskeleton is finalized, a detailed controller for the exoskeleton actuators can be modeled and simulated to test different control strategies (e.g., position, torque, impedance control [30] and adaptive assist-as-needed control [31]).

Step 6 (*Virtual experimentation*)*:* Carry out virtual experiments to study specific "what-if" scenarios (e.g., introduce impaired muscle groups in the model) and generate modifications in the design and control to investigate such cases. We also show how the proposed framework can help quantify the performance of many candidate designs and thus significantly shorten the development life cycle of the exoskeletons.

Below, we present a case study to illustrate the application of the proposed framework to virtually prototype an index finger exoskeleton.

3 Index Finger Exoskeleton Prototyping Case Study

An index finger exoskeleton is chosen as an example since the index finger plays a significant role in hand function [32], and rehabilitation of index finger movement is important during the recovery after stroke. In addition, a hand exoskeleton consists of several similar modules for other fingers, and thus, an analysis of the index finger module would provide overall quantitative performance of the device. We also present virtual experiments where different pathological conditions are simulated.

We developed a preliminary design of the index finger exoskeleton (Figs. 2(*a*) and 2(*b*)). The setup consists of a base to which the exoskeleton and actuators (not shown in figure) are connected. The design supports active assistance of the metacarpophalangeal (MCP), proximal interphalangeal (PIP), and distal interphalangeal (DIP) joints of the index finger in both flexion and extension. The design also has a passive degree-of-freedom (DOF) for abduction and adduction at the MCP joint. The device is actuated using antagonistic tendons connected to the actuators (i.e., exotendons), such that it can be used for both active and passive rehabilitation. In active rehabilitation, finger movements are achieved by the combined efforts of the patient and device, whereas in passive rehabilitation finger movements are achieved by the device entirely. The design has a mechanism to adjust the link lengths for accommodating different hand sizes. The range of motion of the various joints can also be adjusted to accommodate a subject's rehabilitation needs.

We introduced spring elements as links in the design to: (a) make the exoskeleton kinematically and dynamically compatible with the human finger and (b) help accommodate any misalignment between the exoskeleton and finger joint axes of rotation to reduce undesired reaction forces at the human joints. In addition, it is possible to reduce the requirement on the control efforts by introducing optimal compliance. Compliance is introduced to make the interaction with the device more comfortable and may lead to prolonged therapy sessions. Further details regarding the exoskeleton can be found in Ref. [29].

In this case study, we focus on the appropriate choice of the exoskeleton stiffness that would result in best tracking performance with the least joint reaction forces, while obtaining the required muscle excitation and exotendon control input (Sec. 3.2). To this end, we carry out a parametric study to assess the effect of the exoskeleton spring stiffness values (k_1–k_4) (Fig. 2(*c*)) on tracking performance, finger joint reaction forces, and muscle and exotendon forces. Below, we apply the six steps of our framework to the design and analysis of the index finger exoskeleton.

3.1 Initial Modeling. An index finger musculoskeletal model (Fig. 3(*b*)) was first isolated from the upper extremity model (Fig. 3(*a*)) presented by Holzbaur et al. [33] while retaining the wrapping surfaces and four Hill-type musculotendon actuators associated with the index finger. A coupled finger–exoskeleton model (Fig. 2(*c*)) was then developed to closely resemble the

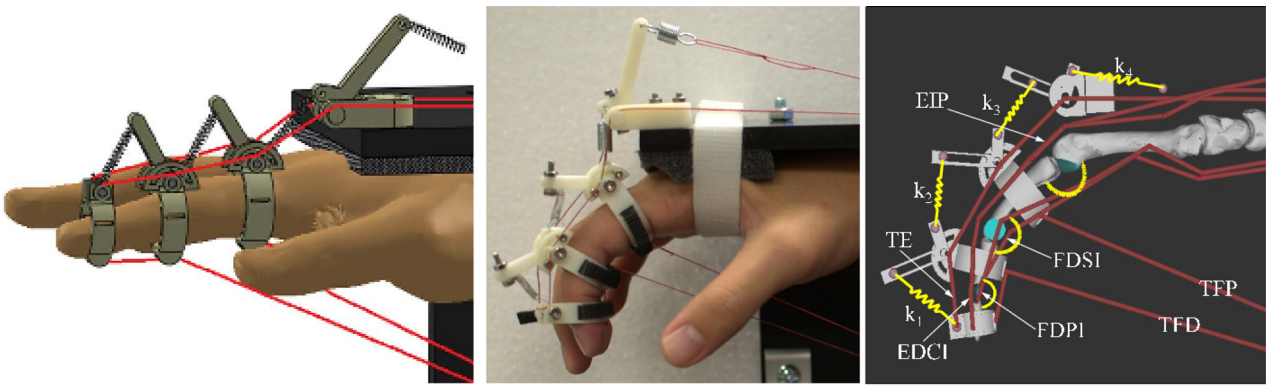

(*a*) (*b*) (*c*)

Fig. 2 Finger–exoskeleton coupled system: (*a*) a 3D model of the developed coupled index finger–exoskeleton system, (*b*) preliminary 3D printed prototype of the device, and (*c*) virtual prototype (musculoskeletal model) used for the simulations. The model has 6DOF consisting of index finger MCP flexion, PIP flexion, DIP flexion, and exoskeleton proximal, middle, and distal link rotation. The three exotendons, the distal flexion tendon (TFD), proximal flexion tendon (TFP), and extension tendon (TE) are also modeled as muscles. The four index finger muscles in the model are FDPI, FDSI, extensor digitorum communis (EDCI), and extensor indicis proprius (EIP).

preliminary prototype of the device. A linear passive rotational stiffness and damping element was added to the three index finger joints to represent the passive contributions from ligaments and other structures [34,35]. Also, linear spring elements (k_1–k_4 in Fig. 2(*c*)) coupling the various exoskeleton links were added to the model. It was assumed that the exoskeleton links are rigidly attached to the finger phalanges and the springs in the design comply to accommodate for any discrepancy in the kinematics that could lead to significant movement of the exoskeleton links. The spring forces between the exoskeleton links were modeled as linear springs, and the passive stiffness at the finger joints was modeled as a rotational spring. So, any misalignment of the exoskeleton generates additional forces due to the stretching of the linear springs, which are eventually transferred to the finger phalanges through the strapped exoskeleton links.

We treated the three exotendons as the force generating elements and modeled them as musculotendon units with their optimal fiber lengths chosen such that the actuators generate a wide range of forces (similar to that of the linear actuators on the device) over the exotendon excursions corresponding to the range of motion of the finger joints. The routing of these musculotendon units is modeled based on the physical routing of the exotendons on the device. Also, since for rehabilitation the required velocities are low, changes in the velocity versus force profile were not needed to achieve the desired force variation. The values for the inertia of the various exoskeleton links in the model are estimated from the CAD model (Fig. 2(*a*)).

We used OpenSim [19] as the computational engine to carry out the musculoskeletal modeling, simulation, and analysis. The musculoskeletal model is a constrained multibody system driven by individual muscle actuators. The model is defined by musculoskeletal geometry, body segment dynamics, and differential equations that describe the muscle contraction dynamics. The model allows for monitoring of a number of internal variables including system lengths (e.g., exotendon and spring lengths), muscle actuator forces, joint reaction forces, and mechanical work.

3.2 Performance Measure Identification. Some of the critical questions related to the design of the proposed index finger exoskeleton are: (a) how does the exoskeleton stiffness affect the

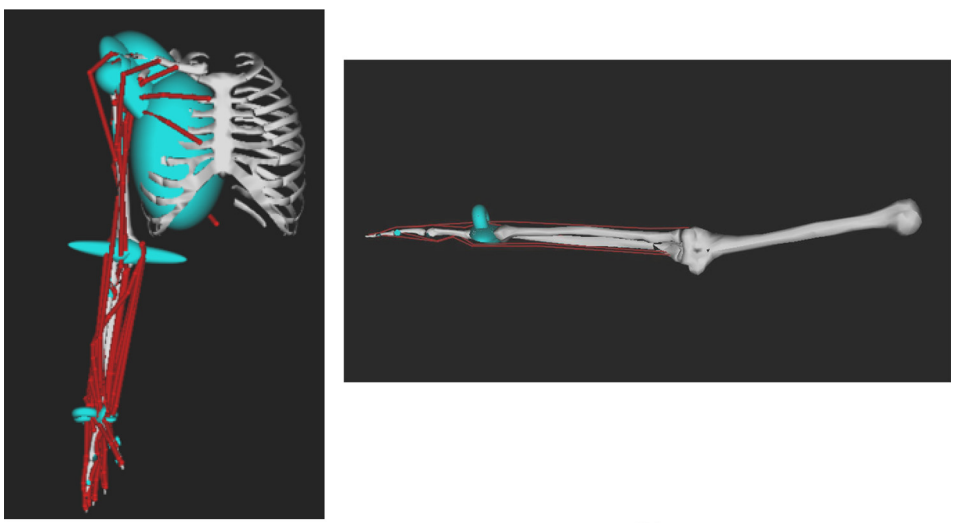

(*a*) (*b*)

Fig. 3 Musculoskeletal model of the human upper limb: (*a*) Stanford VA upper limb model and (*b*) isolated index finger model

motion tracking performance of the device (i.e., how accurately the exoskeleton moves the finger joints relative to the desired finger joint trajectories)? (b) how does the exoskeleton stiffness affect the muscle and exotendon forces during operation? and (c) how does the exoskeleton stiffness affect the joint reaction forces (e.g., should be as low as possible for a comfortable interaction with the device)? We assessed the performance using the following measures: (a) Biomechanical measures consisting of finger joint reaction forces and musculotendon forces, which are important biomechanical factors for a hand exoskeleton [16,29] and (b) Morphological measures quantifying exoskeleton kinematic compatibility (i.e., motion tracking performance) and dynamic compatibility (i.e., exotendon forces that are governed by the spring stiffness chosen for the exoskeleton).

Previous work has shown that human finger joint motions corresponding to certain activities of daily living can be approximated using a sinusoid [36]. Thus, we used a sinusoidal flexion–extension trajectory (Eq. (1)) to be the desired motion and assumed the relative exoskeleton joint angular displacements to be zero as these are small during the motion. A relationship between PIP and DIP joint angles was developed based on hand anatomy [37] and used to constrain the two joint angles as follows:

$$\theta_j = \theta_{m,j}\sin\left(\omega_j t + \phi_j\right),\ j \in \{\text{MCP}, \text{PIP}\}$$
$$\theta_{\text{DIP}} = \frac{2}{3}\theta_{\text{PIP}} \tag{1}$$

where θ_j represents the joint angle; and $\theta_{m,j}$, ω_j, and ϕ_j represent the magnitude, angular frequency, and phase, respectively, of the sinusoidal trajectory for the jth joint.

3.3 Model Fidelity

3.3.1 Moment Arm Experimental Data Fitting. Finger moment arms derived from cadaveric or in vivo studies vary among studies due to differences in the methods used to collect the data and hand sizes [38–41]. In order to evaluate the moment arm accuracy, the experimental data were first normalized and then fitted with a second-order polynomial function. We normalized the moment arms by multiplying it with a ratio of the total index finger length of the musculoskeletal model to the length provided in the respective data set. We only evaluated moment arm fitting functions for the index finger flexors–flexor digitorum profundus (FDPI) at MCP, PIP, and DIP and flexor digitorum sublimis (FDSI) at MCP (Fig. 4), due to the availability of reliable data for these muscles. The fitting results (Table 1) showed that the nonlinear fitting functions accurately represent the experimental moment arm data.

3.3.2 Muscle Moment Arm Optimization. A comparison of the muscle moment arm of the available musculoskeletal model (Fig. 3) with the fitted data (Fig. 4) showed that the two differ significantly. A previous study optimized the shoulder joint moment arms by altering the wrapping object parameters [42]. However, no study has optimized the moment arms by altering both the muscle points (i.e., origin, via, and insertion points) and wrapping object parameters. Thus, we refined the moment arm of muscles individually by altering both the muscle points and wrapping object parameters to minimize the difference between model and experimentally fitted moment arms (Eq. (2)) subjected to upper (ϵ) and lower limits ($-\epsilon$) on the allowable changes ($X - X_0$) in the parameters

$$\min_X J(X) = \sum_{i=1}^{m}\left[\sum_{j=1}^{n}\left[r_{\text{mod}}(\theta_{ij}, X) - r_{\text{exp}}(\theta_{ij})\right]^2\right]$$
$$\text{subject to } -\epsilon \le X - X_0 \le \epsilon \tag{2}$$

where m is the number of joints spanned by the muscle, n is the number of time steps, θ_{ij} is the joint angle of the ith joint at the jth time step, X is the location of muscle points and dimensions of the wrapping objects, and r_{mod} and r_{exp}, are the model and experimentally measured moment arms,

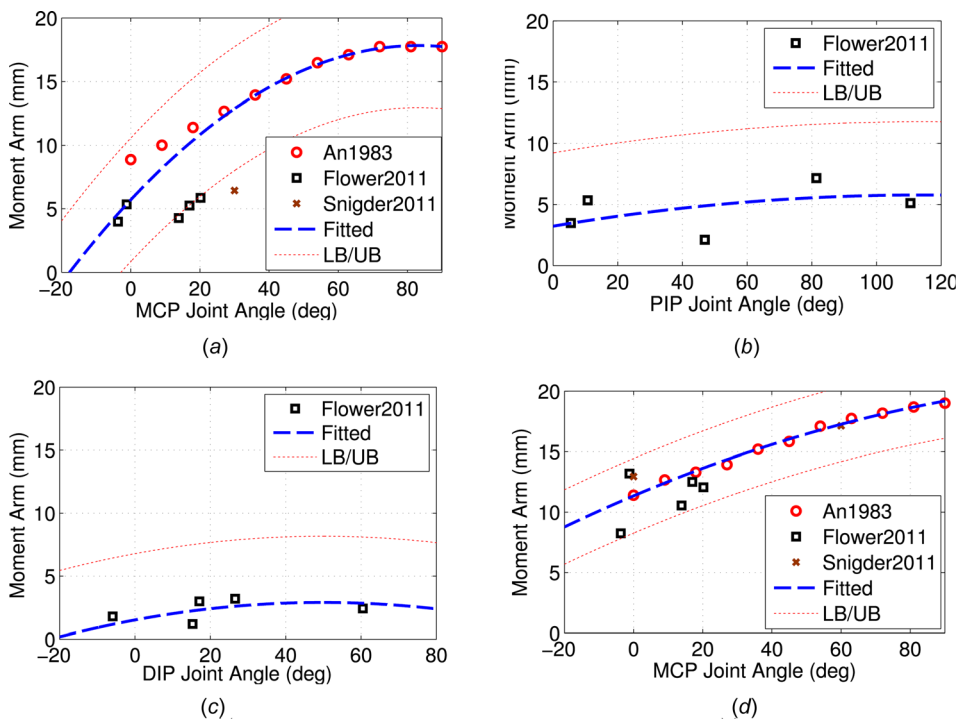

Fig. 4 The fitting results for the index finger flexors at the three joints of the index finger. FDPI muscle at (*a*) MCP, (*b*) PIP, (*c*) DIP, and (*d*) FDSI muscle at MCP. LB and UB represent the upper and lower bound, respectively, on the fitted curve.

Table 1 The goodness-of-fit statistics for the second-order polynomial fitting of the index finger muscles moment arm data

	FDPI			FDSI
Fitting function	MCP	PIP	DIP	MCP
R^2	0.92	0.78	0.75	0.95
Root mean square error (RMSE) (mm)	1.61	0.82	0.66	1.12

respectively. We evaluated the moment arms using OPENSIM and used an interior-point algorithm [43] for the optimization. A MATLAB–OpenSim interface (Fig. 5) was developed to carry out the optimization and is described next.

3.3.3 MATLAB-OpenSim Framework. A MATLAB–OpenSim framework was developed to carry out the optimization of the muscle moment arms (Fig. 5). A MATLAB script writes an OpenSim model and states (joint angles) file with the desired model parameters and states, respectively. The OpenSim application programming interface (API) commands were then invoked from within MATLAB to analyze and write to file the moment arm of each muscle. The model output and fitted results (Fig. 4) were used to evaluate the optimization objective function (Eq. (2)), which was then iteratively optimized by altering the model parameters. Currently, the developed framework is designed to optimize the moment arms. However, the OpenSim API commands can be used to carry out a wide range of analyses.

3.4 Virtual Design and Control. To reproduce the desired trajectory with the coupled optimized model, we used computed muscle control (CMC) in OpenSim to determine both the muscle excitation patterns and exotendon control input to track the desired trajectory. CMC is an efficient algorithm to compute muscle excitation patterns (i.e., actuator control inputs) using static optimization along with feedforward and feedback control to drive the kinematic trajectory of the musculoskeletal model toward a set of desired kinematics [44]. The feedback control used in CMC was a proportional–derivative control with k_p and k_v as the proportional and derivative gains, respectively.

We used the sinusoidal motion (1) as the desired motion for the coupled system ($\ddot{q}_j^*$, $\ddot{q}_k^*$). Lower tracking weights ($w_{\text{exo}} \ll w_{\text{fin}}$ in Eq. (3)) were used for exoskeleton link joint angles and reserve actuators in OpenSim [19] at the various joints to compensate for the assumed motion of the exoskeleton links. We used $w_{\text{exo}} = 0.1$ and $w_{\text{fin}} = 1000$ as the tracking weights in the analysis. We used proportional gain $k_p = 100$ and derivative gain $k_v = 20$ for the CMC feedback control

$$\begin{aligned} \min_{u_i} J(u_i) = &\sum_{i=1}^{7} u_i^2 + \sum_{j=1}^{3} w_{\text{fin}} (\ddot{q}_j^* - \ddot{q}_j)^2 \\ &+ \sum_{k=1}^{3} w_{\text{exo}} (\ddot{q}_k^* - \ddot{q}_k)^2 \\ \text{subject to } & u_i \le u_{i,\max},\ 1 \le i \le 7 \\ & u_i \ge u_{i,\min},\ 1 \le i \le 7 \end{aligned} \tag{3}$$

3.4.1 Parametric Study. A parametric study was carried out to study the effect of exoskeleton stiffness ($k_1 - k_4$) variation on the coupled system performance using the developed MATLAB–OpenSim framework. The stiffness values are varied in the design space, and CMC analysis is carried out to evaluate the system performance metrics. We define three metrics based on the identified performance measures to quantify design performance.

Average finger joint angle root mean square (RMS) error ($\Delta\Theta_f$) is defined as the RMS error between the actual finger joint angle trajectory (θ_a) and the desired finger joint angle trajectory (θ_d) averaged over time and averaged over the number of joints (Eq. (4))

$$\Delta\Theta_f = \frac{1}{N}\sum_{i=1}^{N}\sqrt{\frac{1}{n}\sum_{j=1}^{n}(\theta_a - \theta_d)^2} \tag{4}$$

Preliminary CMC simulation of the system showed that low exoskeleton stiffness leads to oscillation of the exoskeleton links, which could result in destabilizing the system. To quantify this oscillation, we define exoskeleton joint angle metric ($\Delta\Theta_e$) as the standard deviation of the exoskeleton joint angle (θ_{ea}) trajectory averaged over the number of exoskeleton joints (N_e) (Eq. (5)). This metric is intended to quantify the spread of the exoskeleton joint angle trajectory

$$\Theta_e = \sqrt{\frac{1}{N_e}\sum_{i=1}^{N_e}\text{var}(\theta_e)} \tag{5}$$

Average finger joint reaction force (R_f) is defined as the RMS of the resultant force induced at the finger joints averaged over the number of joints (Eq. (6))

$$R_f = \frac{1}{N}\sum_{i=1}^{N}\sqrt{\frac{1}{n}\sum_{j=1}^{n}(f_x^2 + f_y^2 + f_z^2)} \tag{6}$$

We choose a design space of $250\,\text{N/m} \le k_1 \le 750\,\text{N/m}$, $250\,\text{N/m} \le k_2 \le 750\,\text{N/m}$, $250\,\text{N/m} \le k_3 \le 1000\,\text{N/m}$, and $250\,\text{N/m} \le k_4 \le 1100\,\text{N/m}$ for the parametric study, based on preliminary analysis.

3.5 Virtual Experimentation. Once the design parameters for the exoskeleton were evaluated, we carried out several virtual experiments. A hypothesis is setup for each virtual experiment, and a simulation is carried out to verify if it supports the stated hypothesis. The experiments showed how the various pathological conditions can be modeled using musculoskeletal analysis and how the degree of disability and recovery can be quantitatively assessed for each. One important aspect of such experiments is that they could help in assessing and building the missing relationship between the physical and functional aspects of hand function.

3.5.1 Weak Muscle. Muscle weakness may result from either muscle dystrophy [45] or limited neural excitation [46]. We simulated the two scenarios by considering the flexor FDSI to be weak. FDSI muscle was chosen as its force contribution is the highest among all the finger muscles [47,48]. We simulated muscle dystrophy by reducing the maximum isometric strength of the FDSI to 50% of its nominal value. Limited neural excitation was simulated by imposing an upper bound ($u_{\text{FDSI,max}}$ in Eq. (3)) on the allowable excitation in CMC to 5% of the maximum allowable value ($u_{\text{FDSI}} \le 0.05$). We used average muscle or exotendon force change to quantify the degree of disability as it provides a single metric to understand a collective increase or decrease in the muscle or exotendon forces. Average muscle or exotendon force change ($\Delta\bar{f}$) is defined as the difference in muscle or exotendon force, respectively, between the impaired (f_w) and healthy (f_h) models for each muscle averaged over time (Eq. (7)) as

$$\Delta\bar{f} = \frac{1}{M}\sum_{i=1}^{M}\left(\frac{1}{n}\sum_{j=1}^{n}(f_w - f_h)\right) \tag{7}$$

where M represents the number of finger muscles or exotendons in the model. The metric can also be defined for each muscle or exotendon individually.

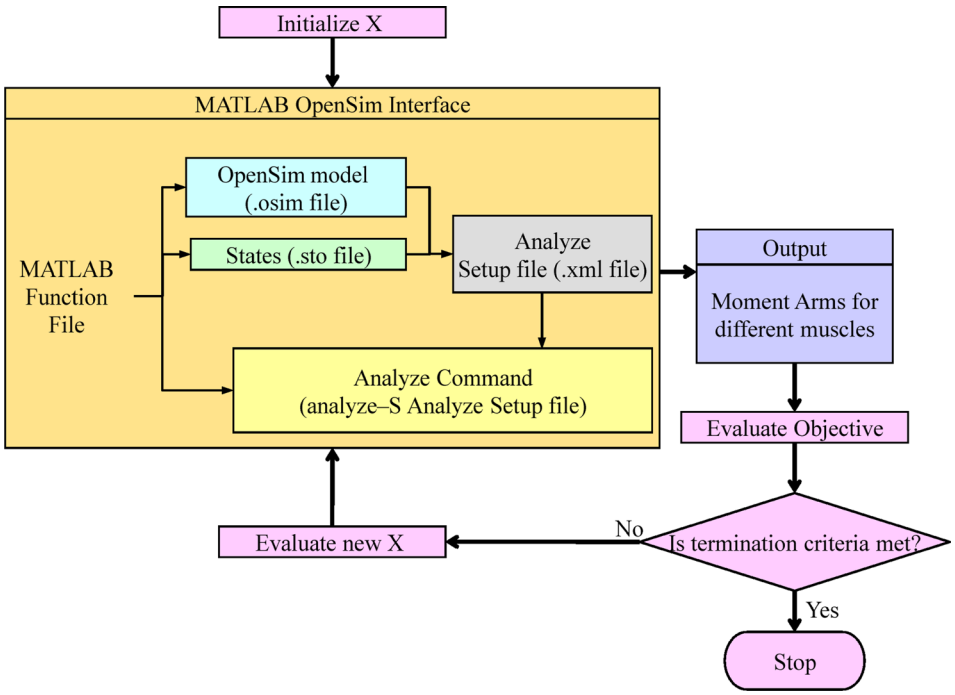

Fig. 5 A MATLAB–OpenSim interface for moment arm optimization. An OpenSim model was generated on-the-fly using MATLAB with the initial parameters. The model was then analyzed for the moment arms using the OpenSim API commands from within MATLAB. The resulting moment arms were used to evaluate the objective function, and the model was optimized iteratively until the termination criteria were met.

Hypothesis (*i*): A finger with an impaired FDSI muscle (either due to muscle dystrophy or limited neural excitation) will generate less average muscle force and require more exotendon force to perform the same motion as compared to a healthy finger. This is because the reduced force contribution of the FDSI muscle to the required net force will be compensated by the exotendons to generate the same motion. Also, the higher the reduction in muscle force, the more exotendon force will be needed. As a result, the relative decrease in muscle or increase in exotendon force will convey the degree of the muscle weakness.

3.5.2 Hypertonicity. Studies have shown that hypertonic (rigid or spastic) muscles lead to increased joint stiffness [49,50]. We simulated hypertonicity by increasing the stiffness at the three finger joints to two times their nominal values. The degree of disability was assessed by using average muscle excitation change,

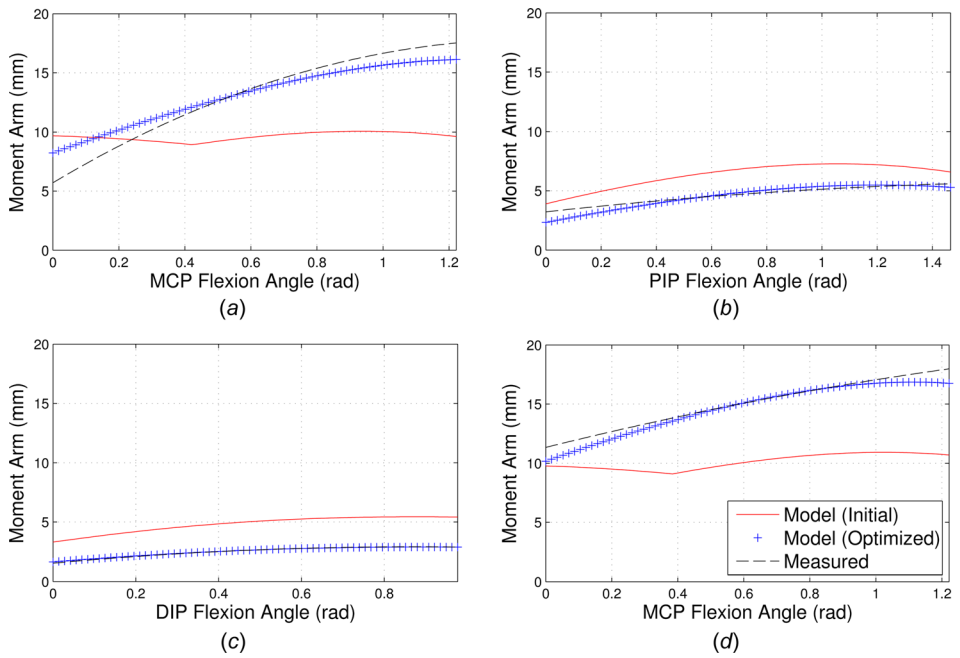

Fig. 6 Optimized model moment arm comparison with the experimentally measured data for FDP muscle at (*a*) MCP joint, (*b*) PIP joint, (*c*) DIP joint, and (*d*) FDS muscle at MCP joint

(*a*) (*b*)

Fig. 7 Comparison of model before (*a*) and after (*b*) muscle moment arm optimization. Alterations in both the origin-, via-, insertion-points and wrapping object dimensions resulted in optimized muscle moment arms.

in addition to average muscle force change. Average muscle excitation or activation change ($\Delta\bar{u}$) is defined as the difference in muscle excitation or activation, respectively, between the impaired (u_w) and healthy (u_h) models for each muscle averaged over time (Eq. (8)) as

$$\Delta\bar{u} = \frac{1}{M}\sum_{i=1}^{M}\left(\frac{1}{n}\sum_{j=1}^{n}(u_w - u_h)\right) \tag{8}$$

Hypothesis (*ii*): A hypertonic finger (increased finger joint stiffness) will require increased muscle excitation (or muscle force) to perform the same motion as compared to a healthy control finger. This is because the increase in finger joint stiffness will require higher muscle forces to achieve the same motion. The increase in the excitation (or force) for this pathology will reflect the degree of hypertonicity.

3.5.3 Imbalanced Muscles. Muscle balance is defined as the relative equality of muscle length, strength, or tone between agonist and antagonist, which is necessary for normal movement and function [51]. Since, the maximum allowable excitation of a muscle for CMC analysis is 1, to simulate muscle imbalance we considered a scenario where the finger flexors exhibit increased excitation ($0.8 \leq u_{\text{flexors}} \leq 1$). We defined joint angle RMS error as another metric to quantify the degree of disability for this case as the finger joint angles were significantly affected by unbalanced muscles resulting in unnatural finger posture. Joint angle RMS error ($\Delta\theta_f$) is defined as the RMS error between the actual joint angle trajectory (θ_a) and the desired joint angle trajectory (θ_d) averaged over time (Eq. (9)) as

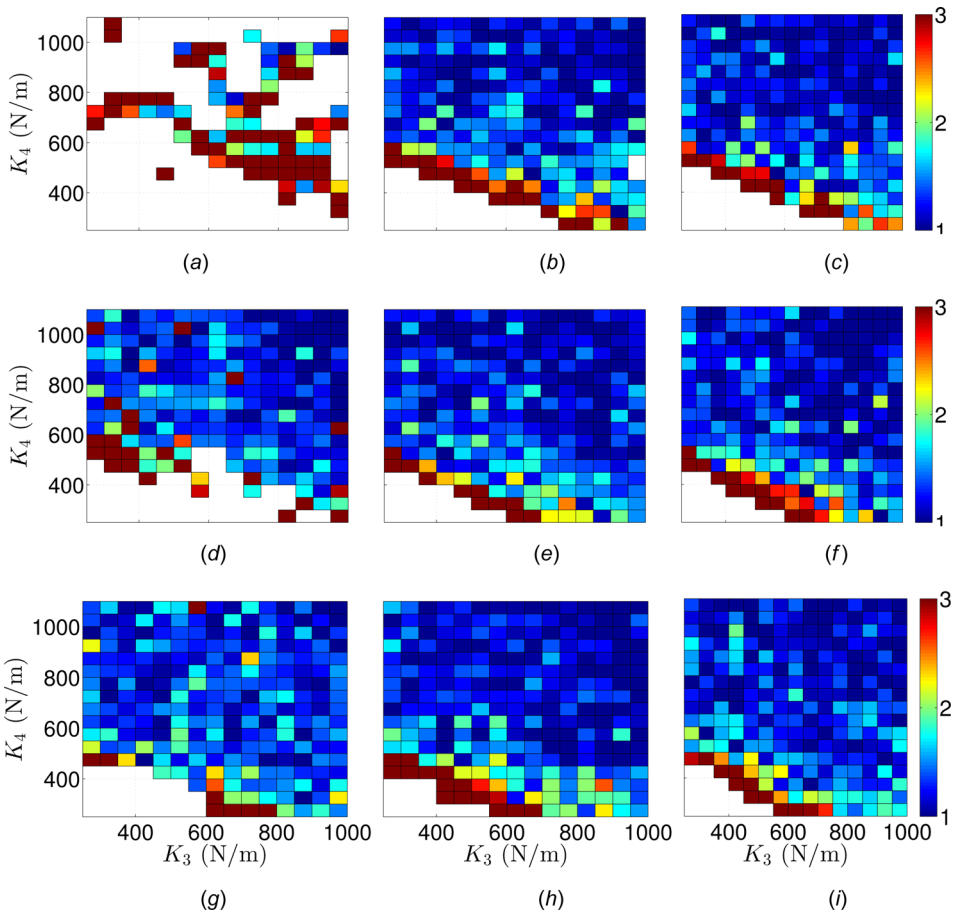

Fig. 8 Exoskeleton joint angle metric mapping for various stiffness values as obtained through the parametric study using CMC analysis for a healthy subject model. The regions with no color indicate that the stiffness combination was found to be infeasible when analyzed using CMC analysis. The unit of the metric is degrees, and all stiffness values are expressed in Newton per meter. The stiffness values k_3 and k_4 are varied in steps of 50 N/m to limit the computational cost. (*a*) $k_1 = 250$, $k_2 = 250$; (*b*) $k_1 = 500$, $k_2 = 250$; (*c*) $k_1 = 750$, $k_2 = 250$; (*d*) $k_1 = 250$, $k_2 = 500$; (*e*) $k_1 = 500$, $k_2 = 500$; (*f*) $k_1 = 750$, $k_2 = 500$; (*g*) $k_1 = 250$, $k_2 = 750$; (*h*) $k_1 = 500$, $k_2 = 750$; and (*i*) $k_1 = 750$, $k_2 = 750$.

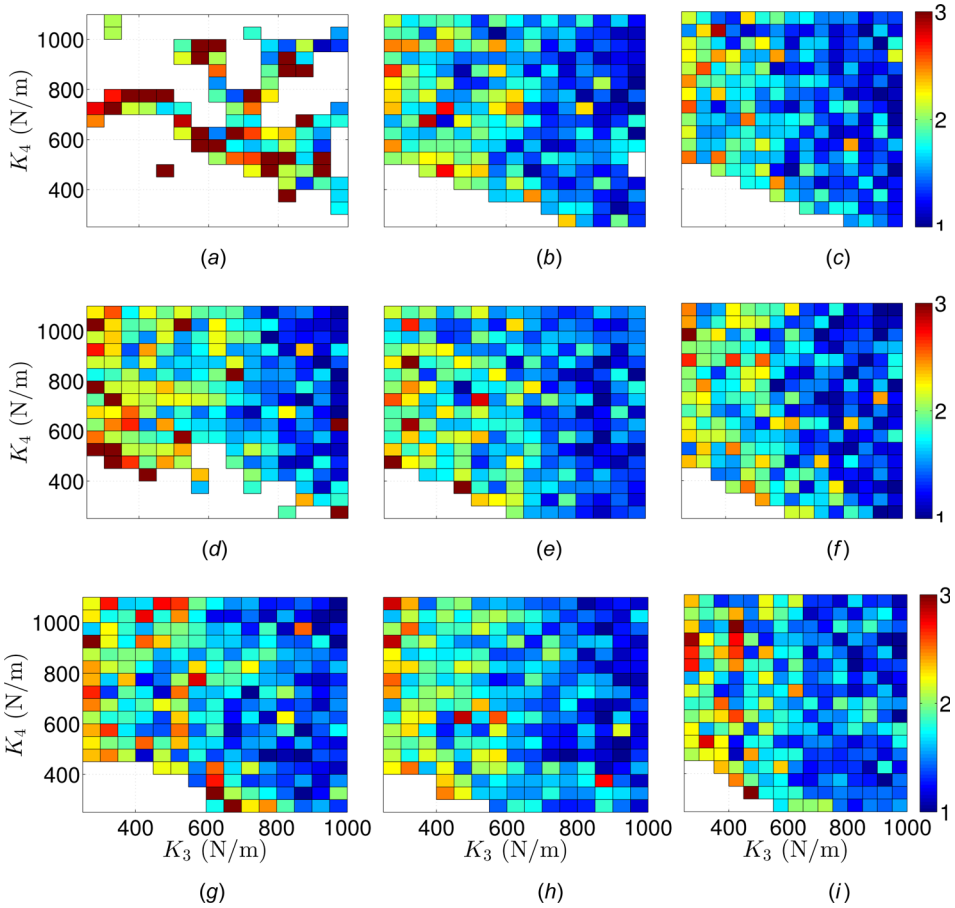

Fig. 9 Finger joint angle error metric mapping for various stiffness values as obtained through the parametric study using CMC analysis for a healthy subject model. The regions with no color indicate that the stiffness combination was found to be infeasible when analyzed using CMC analysis. The unit of the metric is degrees, and all the stiffness values are expressed in Newton per meter. (*a*) $k_1 = 250$, $k_2 = 250$; (*b*) $k_1 = 500$, $k_2 = 250$; (*c*) $k_1 = 750$, $k_2 = 250$; (*d*) $k_1 = 250$, $k_2 = 500$; (*e*) $k_1 = 500$, $k_2 = 500$; (*f*) $k_1 = 750$, $k_2 = 500$; (*g*) $k_1 = 250$, $k_2 = 750$; (*h*) $k_1 = 500$, $k_2 = 750$; and (*i*) $k_1 = 750$, $k_2 = 750$.

$$\Delta\theta_f = \sqrt{\frac{1}{n}\sum_{i=1}^{n}(\theta_a - \theta_d)^2} \tag{9}$$

Hypothesis (*iii*): A finger with imbalanced muscles (increased excitation in finger flexors) will result in poorer tracking of the desired joint angle trajectories compared to a healthy finger. This is because consistently increased forces in the flexor muscles will generate uncoordinated motion at the finger joints and make it difficult to track the desired trajectories. How significantly the tracking is affected will depend on how imbalanced the finger muscles are. Thus, the joint angle RMS error will signify the degree of imbalance in the muscles.

3.5.4 Muscle Contracture. Muscle contracture consists of shortening of muscle length along with an increase in the resistance to passive stretch [52]. We simulated muscle contracture by reducing the optimal fiber length of the FDSI muscle by 10% of its nominal value. The degree of disability was assessed using the average muscle force change.

Hypothesis (*iv*): A finger with a contractured FDSI muscle will result in increased average muscle force as compared to a finger with normal FDSI muscle. This is because a shortened finger muscle will be stretched more to generate the same motion. This excessive stretching of the muscle will result in increased muscle forces. The increase in the muscle force will indicate the amount of extra stretching, which in turn will depend on the degree of muscle contracture.

3.5.5 Simulating Rehabilitation Progress. Finally, virtual experiments were carried out to assess whether a recovering finger can be simulated as a way of estimating the recovery progress quantitatively using the exoskeleton. Improved finger function was simulated by increasing the maximum allowable excitation constraint ($u_{i,\max}$ in Eq. (3)) for the finger muscles during CMC and subsequently, evaluating the required muscle and exotendon forces. Since, with this new constraint higher excitations were allowed for the finger muscles, a redistribution of the muscle and exotendon forces should take place with more forces being applied by the finger muscles. Thus, a recovering finger at various stages of recovery could be simulated using the presented framework along with a quantification of the recovery progress.

Hypothesis (*v*): A finger with a 85% recovered FDSI muscle will generate more active muscle force as compared to one with 15% recovery. This is because larger active forces will be applied by the recovered finger muscles to contribute to the resultant force needed to generate the finger motion.

4 Results

4.1 Model Fidelity. A comparison of the optimized model moment arm with the fitted (experimentally measured) data for the FDP muscle at the MCP, PIP, and DIP joints showed that the model-based estimates were close to the fitted data after optimization (Fig. 6). However, the initial model-based moment arms

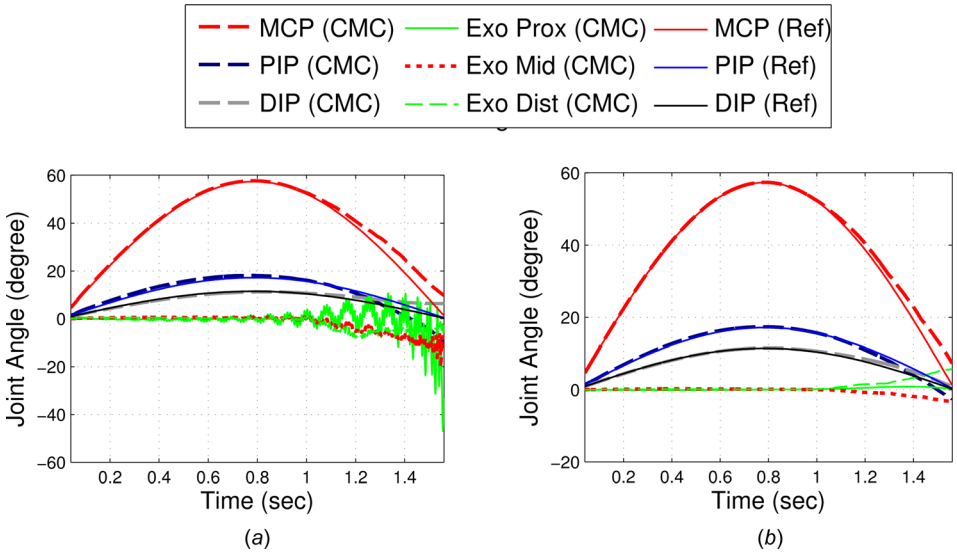

Fig. 10 Joint angle tracking performance for various joints in the system with different exoskeleton stiffnesses as obtained from the CMC analysis for a healthy subject model. (*a*) Low stiffness ($k_1 = 250$, $k_2 = 275$, $k_3 = 500$, and $k_4 = 600$) N/m and (*b*) high stiffness ($k_1 = 800$, $k_2 = 900$, $k_3 = 1000$, and $k_4 = 1100$) N/m. The exoskeleton links show large fluctuations at lower exoskeleton stiffness. Also, there is an appropriate relationship of stiffness among different links of the exoskeleton for kinematic and dynamic compatibility of the exoskeleton with the finger. Increasing exoskeleton stiffness resulted in improved tracking performance. "Ref" refers to the reference trajectory for tracking for the respective joint angle.

were significantly different from the fitted (measured) data. Thus, the optimization improved the model fidelity (Fig. 7).

4.2 Virtual Design and Control

4.2.1 Effect of Stiffness on Tracking Performance. The exoskeleton and finger joint angle metric mappings obtained from the parametric study of the four stiffness values showed the stiffness combinations that result in a stable motion of the exoskeleton and finger joints. The feasible region of the stiffness combination grows as the stiffness value increases (Figs. 8 and 9). In general, all the feasible regions are found to satisfy the following general criterion $k_1 \leq k_2 \leq k_3 \leq k_4$. Also, the performance changes quickly with small stiffness variation both for the exoskeleton and finger joint angle metric, showing the high sensitivity of the kinematics to the stiffness variation. The exoskeleton joint angle metric mapping shows that the performance improves as both the stiffnesses k_3 and k_4 are increased in a similar manner. However, the finger joint angle error metric shows that the performance improves more with increasing k_3 as compared to k_4. This can be because both k_3 and k_4 directly interface with an exoskeleton link. On the other hand, k_3 is closer to the finger joint as compared to k_4. The parametric study helped in understanding this complex relationship between stiffness and joint angle tracking performance.

The plots in time also showed that for the tracking task, the finger joint angles (MCP (CMC), PIP (CMC), and DIP (CMC)) were very close to their respective nominal positions (MCP (Ref), PIP (Ref), and DIP (Ref), Fig. 10). Lower exoskeleton stiffness resulted in larger oscillations in the angular position of exoskeleton links (Exo Prox (CMC), Exo Mid (CMC), and Exo Dist (CMC)), which resulted in a higher exoskeleton joint angle metric. Also, the relationship among different springs' stiffness values in the design defines the kinematic and dynamic compatibility of the exoskeleton with the finger. Furthermore, increasing the exoskeleton stiffness resulted in better tracking of the joint angles as the exoskeleton joint angle fluctuations were reduced. A region with $250 \leq k_1 \leq 500$, $250 \leq k_2 \leq 500$, $500 \leq k_3 \leq 600$, and $600 \leq k_4 \leq 700$ shows a relatively stable performance.

4.2.2 Effect of Stiffness on Joint Reaction Forces. The parametric study showed that the finger joint reaction metric follows a relatively smoother pattern as compared to the exoskeleton and finger joint angle metrics (Fig. 11). This shows that the dynamics of the design is less sensitive to stiffness variation. The finger joint reaction metric is significantly affected by k_3 and is relatively less affected by k_4. This is because the direct reaction forces induced due to k_4 are grounded by the exoskeleton link and does not result in inducing considerable reaction forces at the finger joints. Also, the induced reaction forces at the finger joints in time showed that the magnitude of the forces at finger joint increases with the increase in exoskeleton stiffness (Fig. 12). Here, a region with $250 \leq k_1 \leq 500$, $250 \leq k_2 \leq 500$, $400 \leq k_3 \leq 600$, and $500 \leq k_4 \leq 800$ shows a relatively low joint reaction forces, while being feasible.

4.2.3 Effect of Stiffness on Muscle and Exotendon Forces. The actuator forces showed that forces were induced in the finger muscles (FDSI, FDPI, EDCI, and EIP) due to their passive stretching (Fig. 13). However, the majority of the forces were applied by the exotendons (TFD, TFP, and TE) as in the rehabilitation scenario. The exotendon forces also showed fluctuations in the region where the exoskeleton links were oscillating. In addition, increasing exoskeleton stiffness resulted in an increase in the required exotendon forces, which in turn increases the actuator power requirement. Thus, the design allows for increasing the exoskeleton stiffness without increasing the force requirement on the muscles.

4.2.4 Choice of Optimum Stiffness. Based on the parametric study of the effects of the joint stiffness combination on tracking performance, joint reaction forces, and muscle and exotendon forces, stiffness combination with $k_1 = 275$ and $k_2 = 325$ showed that several feasible solutions can be obtained in the region ($500 \leq k_3 \leq 600$ and $600 \leq k_4 \leq 700$) with satisfactory performance metrics (Fig. 14). However, a trade-off is involved in selecting the stiffness as the requirement of achieving good

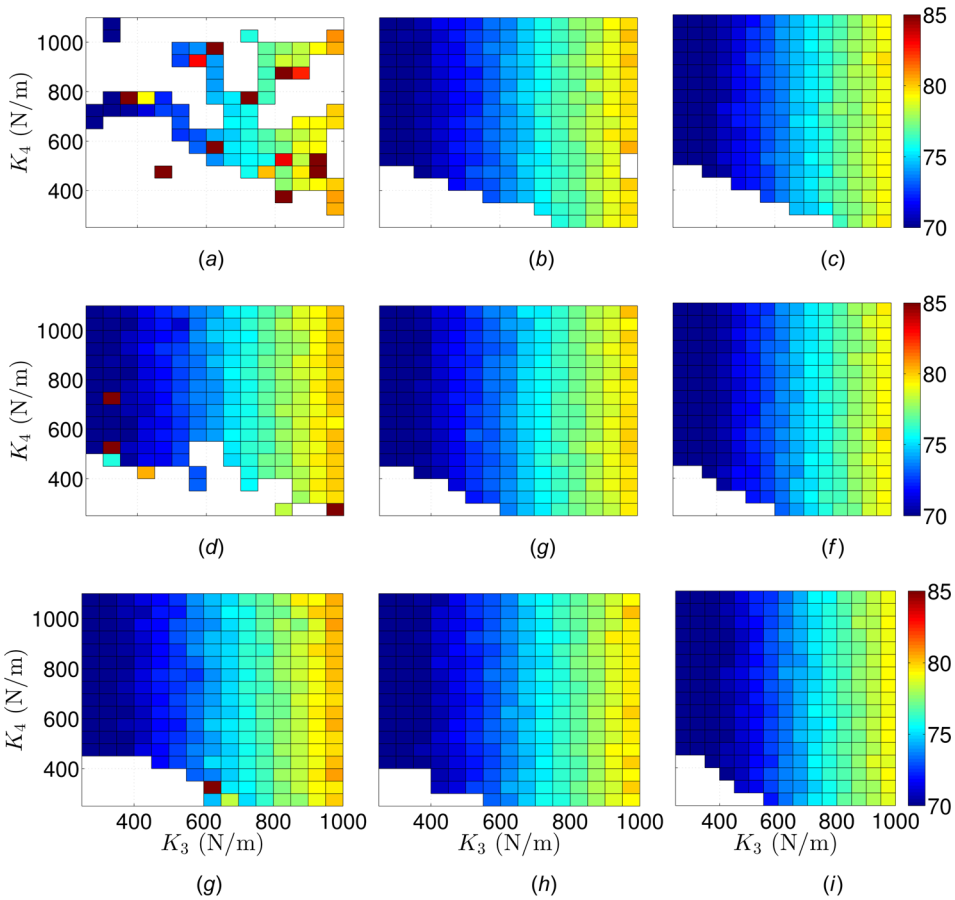

Fig. 11 Finger joint reaction force metric mapping for various stiffness values as obtained through the parametric study using CMC analysis for a healthy subject model. The regions with no color indicate that the stiffness combination was found to be infeasible when analyzed using CMC analysis. The unit of the metric is Newton, and all the stiffness values are expressed in Newton per meter. (*a*) $k_1 = 250$, $k_2 = 250$; (*b*) $k_1 = 500$, $k_2 = 250$; (*c*) $k_1 = 750$, $k_2 = 250$; (*d*) $k_1 = 250$, $k_2 = 500$; (*e*) $k_1 = 500$, $k_2 = 500$; (*f*) $k_1 = 750$, $k_2 = 500$; (*g*) $k_1 = 250$, $k_2 = 750$; (*h*) $k_1 = 500$, $k_2 = 750$; and (*i*) $k_1 = 750$, $k_2 = 750$.

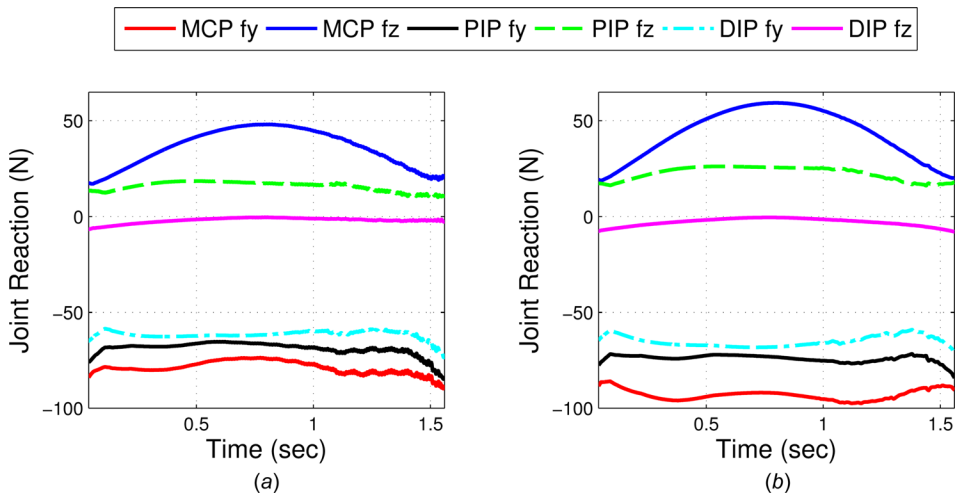

Fig. 12 Joint reactions induced at the various index finger joints with different exoskeleton stiffnesses as obtained from the CMC analysis for a healthy subject model. (*a*) Low stiffness ($k_1 = 250$, $k_2 = 275$, $k_3 = 500$, and $k_4 = 600$) N/m and (*b*) high stiffness ($k_1 = 800$, $k_2 = 900$, $k_3 = 1000$, and $k_4 = 1100$) N/m.

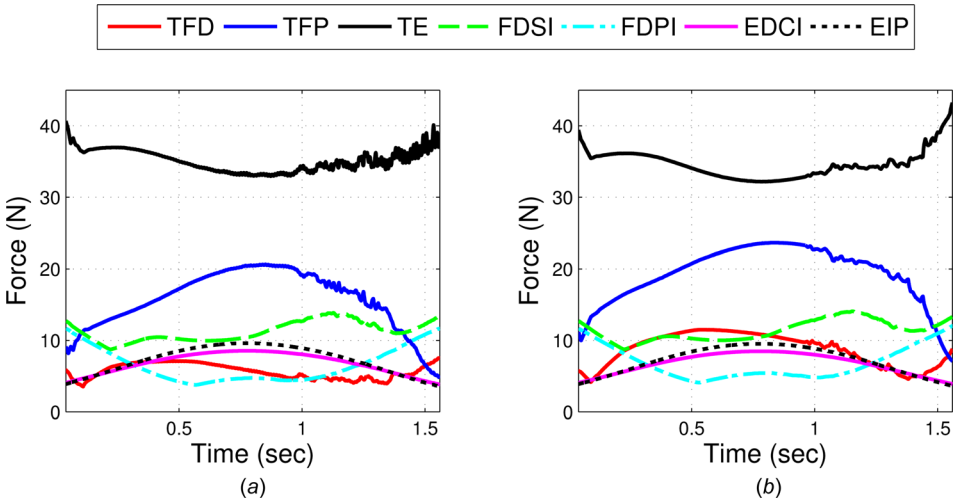

Fig. 13 Actuator (muscle/exotendon) forces needed for tracking with different exoskeleton stiffnesses as obtained from the CMC analysis for a healthy subject model. (*a*) Low stiffness ($k_1 = 250$, $k_2 = 275$, $k_3 = 500$, and $k_4 = 600$) N/m and (*b*) high stiffness ($k_1 = 800$, $k_2 = 900$, $k_3 = 1000$, and $k_4 = 1100$) N/m.

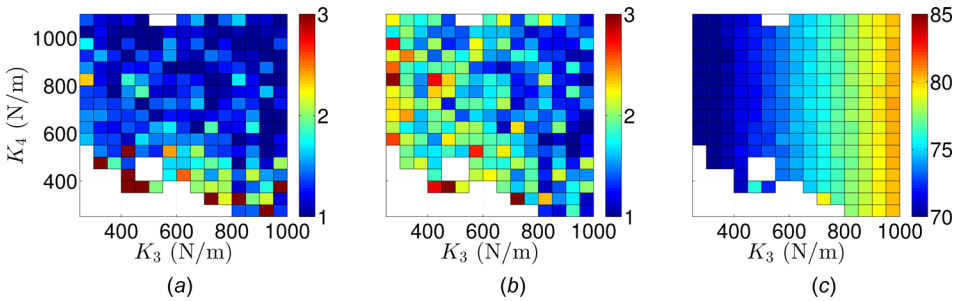

Fig. 14 Performance metric mappings for various stiffness values as obtained through the parametric study using CMC analysis for a healthy subject model with $k_1 = 275$ N/m and $k_2 = 325$ N/m: (*a*) exoskeleton joint angle metric, (*b*) finger joint angle metric, and (*c*) finger joint reaction force metric. The regions with no color indicate that the stiffness combination was found to be infeasible when analyzed using CMC analysis.

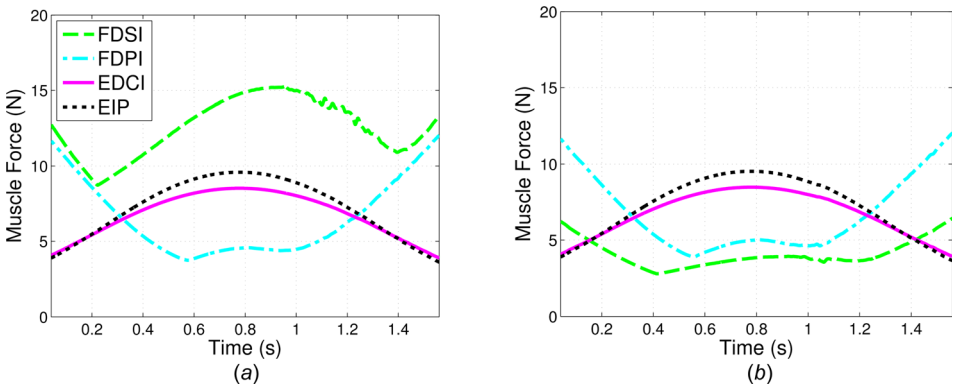

Fig. 15 Muscle force variation during the finger flexion–extension task in a subject with (*a*) healthy muscles and (*b*) weak FDSI muscle due to 50% reduced isometric strength

tracking performance conflicts with the requirement of low finger joint reaction forces. We choose one such optimum candidate ($k_3 = 550$ and $k_4 = 650$) for further analysis of the design, wherein the stability is also maintained in the surrounding region to ensure the robustness of the design against stiffness variation.

4.3 Virtual Experimentation

4.3.1 Weak Muscle. When the muscle strength was reduced to 50% the average FDSI muscle force, the average muscle force (8.28 N) decreased by 25.38% (2.10 N) and average exotendon force (19.04 N) increased by 4.12% (0.7842 N) (Fig. 15(*b*)) as

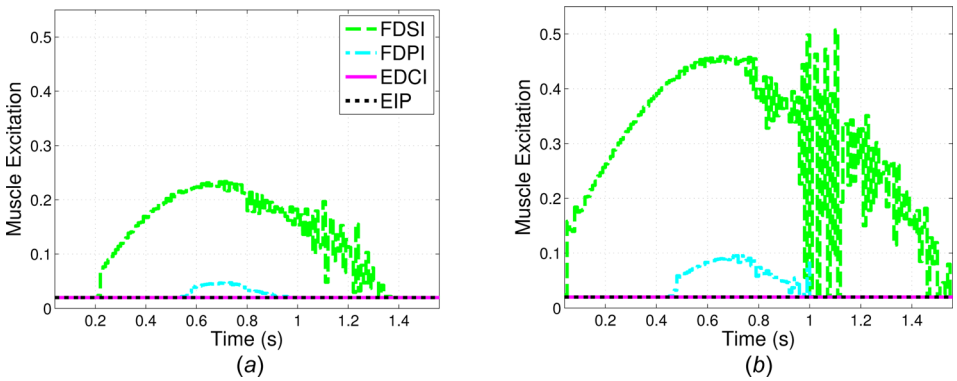

Fig. 16 Muscle excitation variation during the finger flexion–extension task for the four finger muscles in a subject with (*a*) healthy control and (*b*) hypertonicity

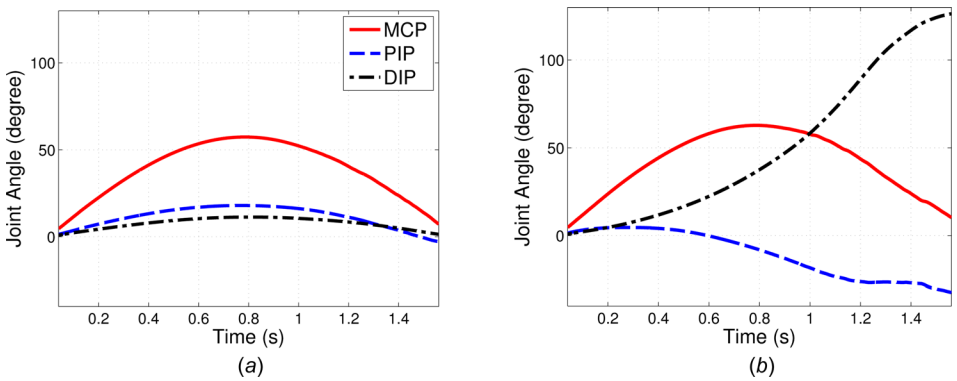

Fig. 17 Finger joint angle tracking results for the finger flexion–extension task in a subject with (*a*) healthy control and (*b*) increased flexor excitation

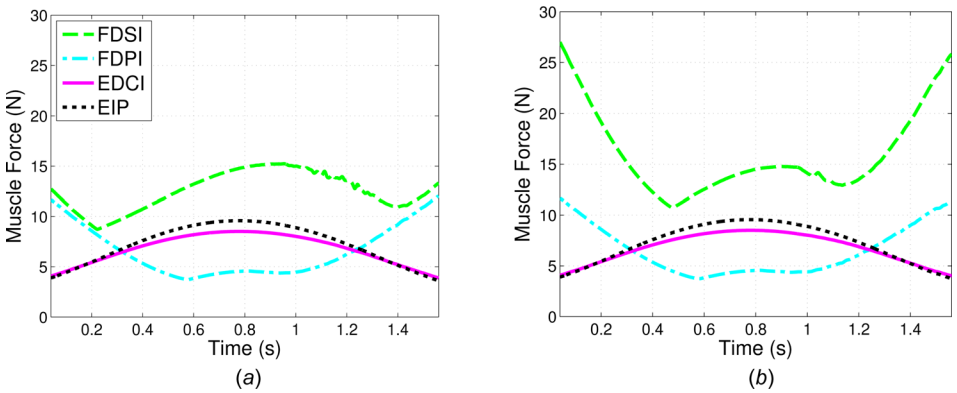

Fig. 18 Muscle forces for the four finger muscles in a subject with (*a*) healthy FDSI muscle and (*b*) FDSI muscle contracture

compared to the forces with healthy FDSI muscle (Fig. 15(*a*)). The average muscle and exotendon force change for the weak FDSI muscle due to limited neural excitation of 5% was −13.76% (−1.1396 N) and 2.47% (+0.4698 N), respectively.

4.3.2 Hypertonicity. The average muscle excitation for a healthy control subject was 0.05 (Fig. 16(*a*)), and the average increase in muscle excitation with two times stiffer joints was 99.99% (0.05) (Fig. 16(*b*)). The average muscle force for a healthy subject was 8.28 N, and the average muscle force change with two times stiffer joints was 32.93% (+2.73 N).

4.3.3 Imbalanced Muscles. With the imbalanced muscles, the actual finger joint angles significantly deviated (Fig. 17(*b*)) compared to the healthy control subject (Fig. 17(*a*)). The RMS error for the MCP, PIP, and DIP joints for the imbalanced muscles was 4.82 deg, 25.53 deg, and 60.26 deg, respectively, as compared to 2.20 deg, 1.24 deg, and 0.55 deg, respectively, for a healthy control subject.

4.3.4 Muscle Contracture. With muscle contracture, the FDSI muscle had higher force toward the beginning and end of the task (Fig. 18(*b*)) as compared to the forces with healthy FDSI muscle (Fig. 18(*a*)). The average muscle force change (8.28 N) for FDSI muscle contracture due to 10% reduction in optimal fiber length was 10.05% (+0.833 N).

4.3.5 Simulating Rehabilitation Progress. With increased recovery, more active forces were applied by the finger muscles

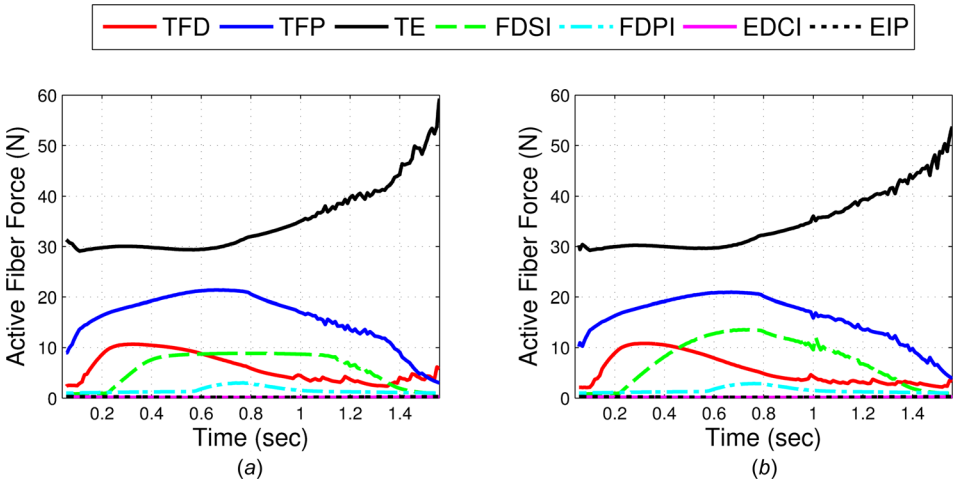

Fig. 19 Active muscle fiber forces in two simulations representing the improving rehabilitation scenario. (*a*) 15% recovery and (*b*) 85% recovery from complete motor disability. Different rehabilitation scenarios are simulated by changing the upper bound on the allowable excitation of the index finger muscles. With increased recovery, more forces are applied by the finger muscles (FDSI muscle carries relatively higher load than the TFD exotendon under 85% recovery)

(especially FDSI) as opposed to the exotendons (TFD and TE) (Fig. 19). Furthermore, the active finger muscle fiber forces (FDSI, FDPI, EDCI, and EIP) were small.

5 Discussion

5.1 Virtual Design and Control. The parametric study showed a process for determining optimum stiffness such that tracking performance is ensured while also minimizing finger joint reaction forces. However, measuring joint reaction forces induced at the finger joints in situ is challenging with a human subject due to the invasive nature of direct measurement and is at best estimated using kinematic and kinetic models with measurements from cadavers [53]. Furthermore, Chao et al. reported only average normalized forces for two specific finger poses as it is difficult to get specific forces induced while performing a task with a cadaver. Chao et al. also stated that in general, the forces become progressively larger from DIP to PIP to MCP. Our simulation shows similar trends. Moran et al. simulated the two poses using the results from Ref. [53] with peak reported forces for one of the poses along one of the directions as −79 N [54]. Our results show comparable peak forces. However, since the finger moves through a large range of motion in our simulation, it is unfitting to directly compare the induced joint reaction forces. This is because the finger joint reaction forces are also significantly affected by the finger pose due to the considerable forces required to stretch the passive structures at the joints and to overcome the effects of damping and system inertia [34,35].

5.2 Virtual Experimentation. For the virtual experiment with a weak muscle, for both the weakness due to muscle dystrophy and limited neural excitation, the average muscle force reduced and the average exotendon force increased, which quantifies the degree of weakness of the muscle and supports hypothesis (i). For the experiment with hypertonicity, both the muscle excitation and force were found to increase, which quantifies the degree of hypertonicity of the finger and supports hypothesis (ii). The experiment with imbalanced muscles showed that the RMS joint angle error is larger with imbalanced muscles as compared to a healthy subject, which quantifies the degree of muscle imbalance and supports hypothesis (iii). The experiment with muscle contracture showed increased FDSI muscle force toward the beginning and end of the task. This is due to the fact that the finger had a low flexion angle at these instants, and thus, higher FDSI muscle force was induced due to passive stretching of the muscle with reduced optimal fiber length. The excessive induced force increased with reduction in the optimal fiber length, and hence, average muscle force change indicated the degree of muscle contracture and supports hypothesis (iv). Hypothesis (v) was also supported, as more active muscle forces were observed with increased recovery.

The virtual experiments provided a means to quantitatively assess the degree of disability and recovery for subjects with different pathological conditions. Also, the coupled system model simulation was able to capture the progressing rehabilitation scenario for virtual experimentation. By inputting the exotendon forces measured on the actual prototype into the musculoskeletal model, the forces applied by the finger muscles can be determined, and thus, rehabilitation improvement can be quantified. In addition, the model can be used to determine the actuation requirements for different rehabilitation conditions. Furthermore, the analysis provided examples of how different pathological conditions can be distinguished using the data captured through the exoskeleton.

5.3 Limitations. Although the models in the framework capture a significant portion of the physics and biomechanics of the coupled human–exoskeleton system, following avenues for improvement still exist: (i) The nonlinear nature of the passive viscoelastic torque [34,55] at the three finger joints could be modeled more accurately; (ii) the current musculoskeletal models do not represent the neuromuscular characteristics of pathologies (e.g., spasticity) accurately [56]; (iii) we do not model the inertial properties of the actuators on the device explicitly as that would require developing new actuator models in OpenSim; (iv) more detailed models of the physical human–robot interaction can be incorporated in the model, which is assumed to be rigid in the present case study; (v) it is assumed that CMC is a reliable way to resolve the actuator forces in a redundantly actuated coupled human–exoskeleton system; (vi) the current model does not capture the actual mechanics of physical and neurological changes that take place in the impaired limb during the rehabilitation process; and (vii) an experimental validation of the forces applied by the exoskeleton and the induced finger joint reaction forces could be carried out to validate the complex simulations. One of the limitations of the framework, in general, is that it requires a reliable musculoskeletal model of the concerned limb, which is not

always readily available, and a model of the exoskeleton to start with. In the future, we plan to address the aforementioned limitations and develop more detailed models of the actuators, which can accurately simulate both the kinematics and dynamics of the actuators on the device. We also plan to carry out a design optimization study with a number of other exoskeleton design parameters including mechanism structure and dimensions of various links. A quantitative metric based on tracking performance, required exoskeleton actuator forces, and induced joint reaction forces will be developed to assess the performance of candidate exoskeleton designs. Finally, the data (e.g., exoskeleton sensors and motion capture) from the actual prototype can be collected to carry out simulations. This data can help in further refining the design and control of the device using the presented framework.

6 Conclusion

We presented a framework for virtual prototyping of exoskeletons by combining musculoskeletal analyses with simulation-based design. With the framework, coupled human–exoskeleton models can be developed for designing, controlling, and testing of exoskeletons using simulation. The framework allows for understanding how the various system design and control parameters affect coupled system performance quantitatively and thereby provides a means to iteratively optimize the performance. We presented biomechanical, morphological, and controller performance measures to quantify rehabilitation, exoskeleton design, and controller performance, respectively. In addition, virtual experiments were conducted using this framework to quantify exoskeleton performance and recovery progress under specific scenarios.

Successful modeling and simulation of the coupled index finger–exoskeleton system demonstrated the features and applications of the proposed framework. Specifically, the case study showed how the exoskeleton actuators (exotendons) can be modeled as muscle–tendon units. The optimization-based approach to modify muscle moment arms by altering the muscle path is an example of model fidelity improvement using experimental measurements. Furthermore, the parametric study carried out for the design variables using CMC showed that the kinematics (joint motion tracking) of the current design is more sensitive to changes in stiffness than its dynamics (muscle, exotendon forces, and joint reaction forces). Finally, the virtual experiments carried out to simulate different pathological scenarios demonstrated the feasibility of quantification of the rehabilitation progress using the current framework. Thus, the case study illustrated how important design decisions for the exoskeleton can be made in a systematic way based on the various performance measures.

Acknowledgment

This work was supported, in part, by the National Science Foundation (NSF) under Grant No. NSF-CPS-1135949.

References

[1] Prange, G., Jannink, M., Groothuis-Oudshoorn, C., Hermens, H., and Ijzerman, M., 2006, "Systematic Review of the Effect of Robot-Aided Therapy on Recovery of the Hemiparetic Arm After Stroke," J. Rehabil. Res. Dev., **43**(2), pp. 171–184.

[2] Takahashi, C. D., Der-Yeghiaian, L., Le, V., Motiwala, R. R., and Cramer, S. C., 2008, "Robot-Based Hand Motor Therapy After Stroke," Brain, **131**(2), pp. 425–437.

[3] Langhorne, P., Coupar, F., and Pollock, A., 2009, "Motor Recovery After Stroke: A Systematic Review," Lancet Neurol., **8**(8), pp. 741–754.

[4] Hwang, C. H., Seong, J. W., and Son, D. S., 2012, "Individual Finger Synchronized Robot-Assisted Hand Rehabilitation in Subacute to Chronic Stroke: A Prospective Randomized Clinical Trial of Efficacy," Clin. Rehabil., **26**(8), pp. 696–704.

[5] Dollar, A., and Herr, H., 2008, "Lower Extremity Exoskeletons and Active Orthoses: Challenges and State-of-the-Art," IEEE Trans. Rob., **24**(1), pp. 144–158.

[6] Hugh, H., 2009, "Exoskeletons and Orthoses: Classification, Design Challenges and Future Directions," J. NeuroEng. Rehabil., **6**, p. 21.

[7] Heo, P., Gu, G., Lee, S., Rhee, K., and Kim, J., 2012, "Current Hand Exoskeleton Technologies for Rehabilitation and Assistive Engineering," Int. J. Precis. Eng. Manuf., **13**(5), pp. 807–824.

[8] Agarwal, P., Fox, J., Yun, Y., O'Malley, M. K., and Deshpande, A. D., 2015, "An Index Finger Exoskeleton With Series Elastic Actuation for Rehabilitation: Design, Control and Performance Characterization," Int. J. Rob. Res., **34**(14), pp. 1747–1772.

[9] Agarwal, P., and Deshpande, A. D., 2015, "Impedance and Force-Field Control of the Index Finger Module of a Hand Exoskeleton for Rehabilitation," IEEE International Conference on Rehabilitation Robotics (ICORR), Singapore, Aug. 11–14, pp. 85–90.

[10] Emken, J., Bobrow, J., and Reinkensmeyer, D., 2005, "Robotic Movement Training as an Optimization Problem: Designing a Controller That Assists Only as Needed," 9th International Conference on Rehabilitation Robotics (ICORR 2005), Chicago, IL, June 28-July 1, pp. 307–312.

[11] Agarwal, P., Fernandez, B. R., and Deshpande, A. D., 2015, "Assist-as-Needed Controllers for Index Finger Module of a Hand Exoskeleton for Rehabilitation," ASME Paper No. DSCC2015-9790.

[12] Gupta, A., O'Malley, M. K., Patoglu, V., and Burgar, C., 2008, "Design, Control and Performance of Ricewrist: A Force Feedback Wrist Exoskeleton for Rehabilitation and Training," Int. J. Rob. Res., **27**(2), pp. 233–251.

[13] Zoss, A. B., Kazerooni, H., and Chu, A., 2006, "Biomechanical Design of the Berkeley Lower Extremity Exoskeleton (BLEEX)," IEEE/ASME Trans. Mechatron., **11**(2), pp. 128–138.

[14] Perry, J. C., Rosen, J., and Burns, S., 2007, "Upper-Limb Powered Exoskeleton Design," IEEE/ASME Trans. Mechatron., **12**(4), pp. 408–417.

[15] Acosta-Marquez, C., and Bradley, D., 2005, "The Analysis, Design and Implementation of a Model of an Exoskeleton to Support Mobility," 9th IEEE International Conference on Rehabilitation Robotics (ICORR 2005), Chicago, IL, June 28-July 1, pp. 99–102.

[16] Chiri, A., Vitiello, N., Giovacchini, F., Roccella, S., Vecchi, F., and Carrozza, M., 2012, "Mechatronic Design and Characterization of the Index Finger Module of a Hand Exoskeleton for Post-Stroke Rehabilitation," IEEE/ASME Trans. Mechatron., **17**(5), pp. 884–894.

[17] Wang, G., 2002, "Definition and Review of Virtual Prototyping," ASME J. Comput. Inf. Sci. Eng., **2**(3), pp. 232–236.

[18] MusculoGraphics, 2016, "SIMM Software Suite," MusculoGraphics, Inc., Santa Rosa, CA, http://www.musculographics.com

[19] Delp, S., Anderson, F., Arnold, A., Loan, P., Habib, A., John, C., Guendelman, E., and Thelen, D., 2007, "OpenSim: Open-Source Software to Create and Analyze Dynamic Simulations of Movement," IEEE Trans. Biomed. Eng., **54**(11), pp. 1940–1950.

[20] AnyBody Technology, 2016, "The AnyBody Modeling System," AnyBody Technology A/S, Aalborg, Denmark, http://www.anybody tech.com

[21] LifeModeler, 2016, "Bringing Simulation to Life," LifeModeler Inc., San Clemente, CA, http://www.lifemodeler.com

[22] Edmund, C., Robert, A., Hiroaki, Y., Jonathan, L., and Naoki, H., 2007, "Virtual Interactive Musculoskeletal System (VIMS) in Orthopaedic Research, Education and Clinical Patient Care," J. Orthop. Surg. Res., **2**(1), pp. 25–40.

[23] Agarwal, P., Narayanan, M., Lee, L., Mendel, F., and Krovi, V., 2010, "Simulation-Based Design of Exoskeletons Using Musculoskeletal Analysis," ASME Paper No. DETC2010-28572.

[24] Cho, K., Kim, Y., Yi, D., Jung, M., and Lee, K., 2012, "Analysis and Evaluation of a Combined Human-Exoskeleton Model Under Two Different Constraints Condition," International Summit on Human Simulation (ISHS), St. Pete Beach, FL, May 23–25.

[25] Zhou, L., Bai, S., Andersen, M. S., and Rasmussen, J., 2015, "Modeling and Design of a Spring-Loaded, Cable-Driven, Wearable Exoskeleton for the Upper Extremity," Model. Identif. Control, **36**(3), pp. 167–177.

[26] Ferrati, F., Bortoletto, R., and Pagello, E., 2013, "Virtual Modelling of a Real Exoskeleton Constrained to a Human Musculoskeletal Model," Biomimetic Biohybrid Syst., **8064**, pp. 96–107.

[27] Agarwal, P., Kuo, P., Neptune, R. R., and Deshpande, A. D., 2013, "A Novel Framework for Virtual Prototyping of Rehabilitation Exoskeletons," IEEE International Conference on Rehabilitation Robotics, (ICORR), Seattle, WA, June 24–26.

[28] Agarwal, P., Kuo, P., Neptune, R. R., and Deshpande, A. D., 2013, *Integration of Musculoskeletal Analysis With Engineering Design for Virtual Prototyping of Exoskeletons*, American Society of Biomechanics, Omaha, NE.

[29] Agarwal, P., Hechanova, A., and Deshpande, A., 2013, "Kinematics and Dynamics of a Biologically Inspired Index Finger Exoskeleton," ASME Paper No. DSCC2013-3893.

[30] Hogan, N., 1984, "Impedance Control: An Approach to Manipulation," American Control Conference (ACC), San Diego, CA, June 6–8, pp. 304–313.

[31] Cai, L. L., Fong, A. J., Liang, Y., Burdick, J., and Edgerton, V. R., 2006, "Assist-as-Needed Training Paradigms for Robotic Rehabilitation of Spinal Cord Injuries," IEEE International Conference on Robotics and Automation (ICRA 2006), Orlando, FL, May 15–19, pp. 3504–3511.

[32] Jones, L. A., and Lederman, S. J., 2006, *Human Hand Function*, Oxford University Press, New York.

[33] Holzbaur, K., Murray, W., Gold, G., and Delp, S., 2007, "Upper Limb Muscle Volumes in Adult Subjects," J. Biomech., **40**(4), pp. 742–749.

[34] Kuo, P. H., and Deshpande, A., 2012, "Muscle-Tendon Units Provide Limited Contributions to the Passive Stiffness of the Index Finger Metacarpophalangeal Joint," J. Biomech., **45**(15), pp. 2531–2538.

[35] Deshpande, A., Gialias, N., and Matsuoka, Y., 2012, "Contributions of Intrinsic Visco-Elastic Torques During Planar Index Finger and Wrist Movements," IEEE Trans. Biomed. Eng., **59**(2), pp. 586–594.

[36] Karnati, N., Kent, B. A., and Engeberg, E. D., 2013, "Bioinspired Sinusoidal Finger Joint Synergies for a Dexterous Robotic Hand to Screw and Unscrew Objects With Different Diameters," IEEE/ASME Trans. Mechatron., **18**(2), pp. 612–623.
[37] Rijpkema, H., and Girard, M., 1991, "Computer Animation of Knowledge-Based Human Grasping," ACM SIGGRAPH Computer Graphics, **25**(4), pp. 339–348.
[38] An, K., Ueba, Y., Chao, E., Cooney, W., and Linscheid, R., 1983, "Tendon Excursion and Moment Arm of Index Finger Muscles," J. Biomech., **16**(6), pp. 419–425.
[39] Fowler, N., Nicol, A., Condon, B., and Hadley, D., 2001, "Method of Determination of Three Dimensional Index Finger Moment Arms and Tendon Lines of Action Using High Resolution MRI Scans," J. Biomech., **34**(6), pp. 791–797.
[40] Martin, J., Latash, M., and Zatsiorsky, V., 2012, "Effects of the Index Finger Position and Force Production on the Flexor Digitorum Superficialis Moment Arms at the Metacarpophalangeal Joints: A Magnetic Resonance Imaging Study," Clin. Biomech., **27**(5), pp. 453–459.
[41] Snijders, J., Visser, J., Korstanje, J., Selles, R., and Veeger, H., 2011, "Estimation of In-Vivo Muscle Moment Arms Around the MCP Joint Using Ultrasound," Master's thesis, Delft University of Technology, Delft, The Netherlands.
[42] Gatti, C., and Hughes, R., 2009, "Optimization of Muscle Wrapping Objects Using Simulated Annealing," Ann. Biomed. Eng., **37**(7), pp. 1342–1347.
[43] Byrd, R., Hribar, M., and Nocedal, J., 1999, "An Interior Point Algorithm for Large-Scale Nonlinear Programming," SIAM J. Optim., **9**(4), pp. 877–900.
[44] Thelen, D., and Anderson, F., 2006, "Using Computed Muscle Control to Generate Forward Dynamic Simulations of Human Walking From Experimental Data," J. Biomech., **39**(6), pp. 1107–1115.
[45] Emery, A. E., 2002, "The Muscular Dystrophies," Lancet, **359**(9307), pp. 687–695.
[46] Stokes, M., and Young, A., 1984, "The Contribution of Reflex Inhibition to Arthrogenous Muscle Weakness," Clin. Sci., **67**(1), pp. 7–14.
[47] Brand, P. W., and Hollister, A., 1999, *Clinical Mechanics of the Hand*, Mosby, St. Louis, MO.
[48] Vigouroux, L., Quaine, F., Labarre-Vila, A., and Moutet, F., 2006, "Estimation of Finger Muscle Tendon Tensions and Pulley Forces During Specific Sport-Climbing Grip Techniques," J. Biomech., **39**(14), pp. 2583–2592.
[49] Wu, Y.-N., Park, H. S., Ren, Y., Gaebler-Spira, D., Chen, J.-J., and Zhang, L.-Q., 2006, "Measurement of Elbow Spasticity in Stroke Patients Using a Manual Spasticity Evaluator," IEEE Engineering in Medicine and Biology Society (EMBS '06), New York, Aug. 30–Sept. 3, pp. 3974–3977.
[50] Peng, Q., Shah, P., Selles, R. W., Gaebler-Spira, D. J., and Zhang, L.-Q., 2004, "Measurement of Ankle Spasticity in Children With Cerebral Palsy Using a Manual Spasticity Evaluator," IEEE Engineering in Medicine and Biology Society (IEMBS '04), San Francisco, CA, Sept. 1–5, pp. 4896–4899.
[51] Page, P., Frank, C. C., and Lardner, R., 2010, *Assessment and Treatment of Muscle Imbalance*, Human Kinetics, Champaign, IL.
[52] O'Dwyer, N. J., Ada, L., and Neilson, P. D., 1996, "Spasticity and Muscle Contracture Following Stroke," Brain, **119**(5), pp. 1737–1749.
[53] Chao, E., Opgrande, J., and Axmear, F., 1976, "Three-Dimensional Force Analysis of Finger Joints in Selected Isometric Hand Functions," J. Biomech., **9**(6), pp. 387–396.
[54] Moran, J. M., Hemann, J. H., and Greenwald, A. S., 1985, "Finger Joint Contact Areas and Pressures," J. Orthop. Res., **3**(1), pp. 49–55.
[55] Milner, T., and Cloutier, C., 1998, "Damping of the Wrist Joint During Voluntary Movement," Exp. Brain Res., **122**(3), pp. 309–317.
[56] Given, J., Dewald, J., and Rymer, W., 1995, "Joint Dependent Passive Stiffness in Paretic and Contralateral Limbs of Spastic Patients With Hemiparetic Stroke," J. Neurol. Neurosurg. Psychiatry, **59**(3), pp. 271–279.